JACS
JOURNAL OF THE AMERICAN CHEMICAL SOCIETY

Article

pubs.acs.org/JACS

Searching the Hearts of Graphene-like Molecules for Simplicity, Sensitivity, and Logic

Sara Sangtarash,[*,†,§] Cancan Huang,[‡,§] Hatef Sadeghi,[†,§] Gleb Sorohhov,[‡] Jürg Hauser,[‡] Thomas Wandlowski,[‡] Wenjing Hong,[*,‡] Silvio Decurtins,[‡] Shi-Xia Liu,[*,‡] and Colin J. Lambert[*,†]

[†]Quantum Technology Centre, Lancaster University, Lancaster LA1 4YB, U.K.

[‡]Department of Chemistry and Biochemistry, University of Bern, CH-3012 Bern, Switzerland

Supporting Information

ABSTRACT: If quantum interference patterns in the hearts of polycyclic aromatic hydrocarbons could be isolated and manipulated, then a significant step toward realizing the potential of single-molecule electronics would be achieved. Here we demonstrate experimentally and theoretically that a simple, parameter-free, analytic theory of interference patterns evaluated at the mid-point of the HOMO−LUMO gap (referred to as M-functions) correctly predicts conductance ratios of molecules with pyrene, naphthalene, anthracene, anthanthrene, or azulene hearts. M-functions provide new design strategies for identifying molecules with phase-coherent logic functions and enhancing the sensitivity of molecular-scale interferometers.

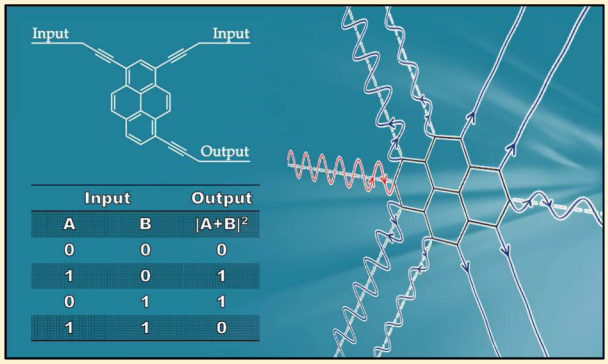

INTRODUCTION

Single-molecule electronic junctions are of interest not only for their potential to deliver logic gates, sensors, and memories with ultra-low power requirements and sub-10-nm device footprints, but also for their ability to probe room-temperature quantum properties at a molecular scale. For example, when a single molecule is attached to metallic electrodes, de Broglie waves of electrons entering the molecule from one electrode and leaving through the other form complex interference patterns inside the molecule.[1−3] Currently there is intense interest in utilizing these patterns in the optimization of single-molecule device performance. Indeed, electrons passing through single molecules have been demonstrated to remain phase coherent, even at room temperature,[3−5] and a series of theoretical and experimental studies have shown that their room-temperature electrical conductance is influenced by quantum interference (QI).[6−19]

In practice, the task of identifying and harnessing quantum effects is hampered because transport properties are strongly affected by the method used to anchor single molecules to electrodes.[20−30] This makes it difficult to identify simple design rules for optimizing the electronic properties of single molecules. Furthermore, few analytic formulas are available, which means that pre-screening of molecules often requires expensive numerical simulations. In what follows, our aim is to introduce a new concept for elucidating QI patterns within the hearts of molecules, caused by electrons entering the molecule with energies E near the mid-point of the HOMO−LUMO (H-L) gap. We refer to these mid-gap interference patterns as M-functions. The approach is intuitive and leads to a simple, parameter-free, analytical description of molecules with polycyclic aromatic hydrocarbon (PAH) cores, which agrees with experiment to an accuracy comparable with that of *ab initio* calculations.

A typical single-molecule junction involves metallic electrodes connected via linker groups to the heart (i.e., core) of the molecule. Figure 1 shows two such molecules, with a common

Figure 1. Two molecules **P1** and **P2** with common pyrene hearts but different connectivities to gold electrodes. (See Figure 2 for more details of the numbering convention used in this study. This does not correspond to the usual chemical numbering convention, but it is convenient analytically and allows us to assign labels to all atoms.)

pyrene-based heart, connected by acetylene linkers to gold electrodes. Such PAHs are attractive for molecular electronics[31−35] because they are defect-free and provide model systems for electron transport in graphene, treated as an infinite alternant PAH.[36,37] As part of our demonstration of the utility of M-functions, we present mechanically controlled break-junction (MCBJ) measurements of the electrical conductance of these molecules. **P1** and **P2** are examples of molecules with identical hearts but different connectivities. **P1** is connected to

Received: June 24, 2015
Published: August 19, 2015

DOI: 10.1021/jacs.5b06558
J. Am. Chem. Soc. 2015, 137, 11425−11431

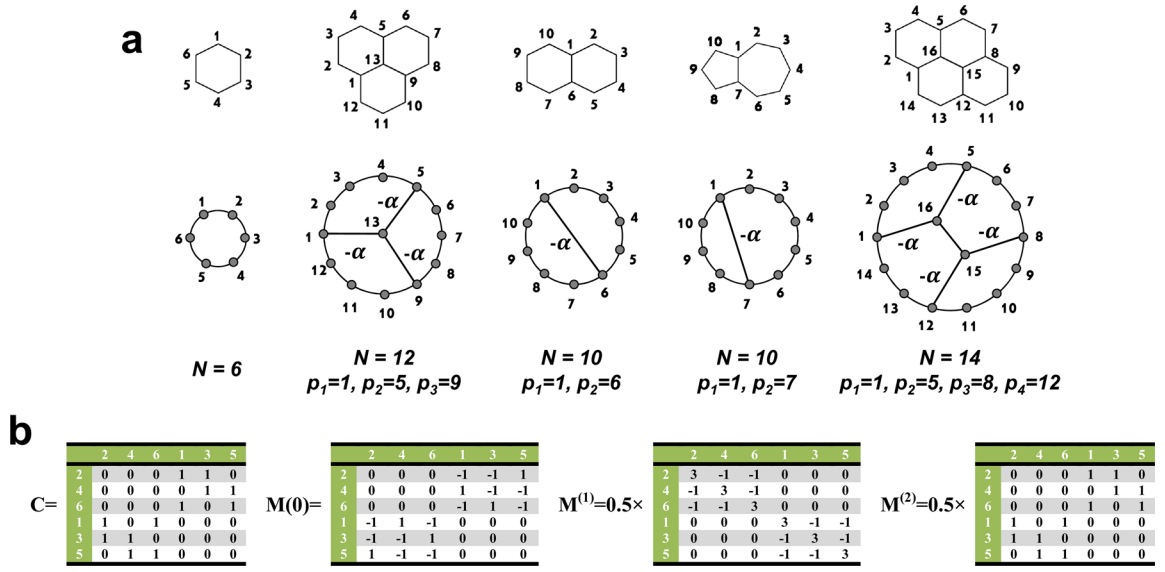

Figure 2. Examples of bipartite and non-bipartite molecules and their lattice representation. (a) The upper row shows lattice representations of a benzene ring, a phenalenylium cation, naphthalene, azulene, and pyrene. The lower row shows connectivity-equivalent representations of these lattices, which can be viewed as rings of peripheral sites, perturbed by the presence of additional bonds to sites p1, p2, etc. Notice that all lattices except azulene are bipartite (i.e., odd-numbered sites are connected to even-numbered sites only). (b) The connectivity table **C** of a benzene ring and all contributions to eq 3 for the benzene M-function. Notice that **C** is block off-diagonal, and as a consequence (see eqs (42) and (46) of the SI), $\mathbf{M(0)}$ and $\mathbf{M}^{(2)}$ are also block off-diagonal, whereas $\mathbf{M}^{(1)}$ is block diagonal.

acetylene linker groups at positions labeled 2 and 9, whereas **P2** is connected at positions 3 and 10.

The amplitude of the interference pattern on an atomic orbital i due to an electron of energy E entering a core at orbital j will be denoted by the M-function $M_{i,j}(E)$. In what follows, it will be convenient to introduce the dimensionless energy E_M, which measures the electron energy relative to the middle of the H-L gap, E_{HL}, in units of the half-width of the H-L gap. If E_H (E_L) is the energy of the HOMO (LUMO) of the core of the molecule, we define the dimensionless energy $E_M = (E - E_{HL})/\delta_{HL}$, where $\delta_{HL} = (E_H - E_L)/2$ and $E_{HL} = (E_H + E_L)/2$. For PAHs represented by bipartite lattices possessing a symmetric energy spectrum and a filled HOMO, the mid-gap energy $E_{HL} = 0$ lies at the center of the spectrum, and the mid-gap interference patterns obey simple rules.[3] More generally, mid-gap transport involves interference at finite E_{HL}, and therefore in what follows, we generalize these rules to encompass interference patterns at all energies within the gap. As shown below, this distinction is particularly important for non-symmetric molecules such as azulene, for which conventional rules for QI break down.[38] When E is close to E_H or E_L (i.e., $E_M = \pm 1$), a Breit−Wigner description based on a HOMO or LUMO resonance is relevant, and therefore one might be tempted to suppose that, near the mid-gap, a description based on a superposition of HOMO and LUMO levels would suffice. Such a description would not be accurate, because at $E_M = 0$, states such as HOMO−1, LUMO+1, etc. make comparable contributions. From the viewpoint of mid-gap quantum transport, such resonances are a distraction, and therefore M-functions are defined such that these irrelevancies are removed.

■ ANALYTIC FORMULAS FOR M-FUNCTIONS

Mathematically we define $M_{i,j}(E) = D(E)G_{i,j}(E)$, where $G_{i,j}(E)$ is the i,jth element of the Green's function, $G(E) = (E - H)^{-1}$, of the Hamiltonian H describing the isolated core and $D(E)$ is a function chosen to cancel divergencies of $G(E)$ which arise when E coincides with an eigenvalue of H. In the absence of degeneracies, it is convenient to choose $D(E)$ to be proportional to the determinant of $(E - H)$. (See the Supporting Information (SI) for more details, along with a list of M-function properties.)

In what follows we shall construct an intuitive description of mid-gap transport, which in its simplest form is parameter-free and describes how connectivity alone can be used to predict the interference patterns created by electrons of energy E_{HL} passing through the heart of PAHs. When linker groups, which are weakly coupled to orbitals i and j, are in contact with metallic electrodes whose Fermi energy E_F lies at the mid-gap E_{HL}, the resulting (low-temperature) electrical conductance $\sigma_{i,j}$ is proportional to $[M_{i,j}(E_{HL})]^2$.[1,3] Therefore, the ratio of two such conductances (associated with links i and j or l and m) is given by the mid-gap ratio rule (MRR):

$$\sigma_{i,j}/\sigma_{l,m} = [M_{i,j}(E_{HL})/M_{l,m}(E_{HL})]^2 \quad (1)$$

We report MCBJ measurements of the conductances of molecules **P1** and **P2** and show that their statistically most probable conductances obey the MRR. We also demonstrate that the MRR agrees with literature measurements of molecules with naphthalene, anthracene, anthanthrene, and azulene hearts. This is a remarkable result, since M-functions and the mid-gap energy E_{HL} contain no information about the electrodes. This agreement between experiment and the MRR is evidence that, in these experiments, the Fermi energy of the electrodes lies close to the mid-gap energy. Having demonstrated the predictive nature of M-functions, we further discuss their utility by showing that M-functions lead to new design strategies for identifying phase-coherent logic functions and for increasing the sensitivity of molecular-scale interferometers.

In general, M-functions depend on the parameters describing the underlying Hamiltonian H of the core. However, for the

DOI: 10.1021/jacs.5b06558
J. Am. Chem. Soc. 2015, 137, 11425−11431

purpose of calculating the contribution to interference patterns from π-orbitals, graphene-like cores can be represented by lattices of identical sites with identical couplings, whose Hamiltonian H is simply proportional to a parameter-free connectivity matrix C. In this case, for electrons of energy E entering the core at site i and exiting at site j, the M-function $M_{ij}(E)$ is also parameter-free and depends on connectivity alone.

As an example, consider a ring of N sites, labeled by integers which increase sequentially in a clockwise direction, as shown in Figure 2. For a benzene ring (where $N = 6$), Figure 2b shows the corresponding connectivity table $\mathbf{C}$, obtained by placing a "1" in all entries for which a connection exists between neighboring sites in the ring. In the simplest π-orbital description of such a ring, where neighboring sites are connected by couplings $(-\gamma)$, the Hamiltonian H is related to the connectivity matrix $\mathbf{C}$ by $H = -\gamma\mathbf{C}$, and as discussed in the SI, the M-function of the ring is given by[1,3]

$$M_{ij}(E) = \cos k(|j - i| - N/2) \tag{2}$$

where $k(E) = \cos^{-1}(-E/2\gamma)$. Without loss of generality, the parameter γ will be set to unity, because it cancels in the MRR, yielding a parameter-free theory. In this case, $E_H = -1$, $E_L = 1$, $E_{HL} = 0$, and the dimensionless energy is $E_M = E$. For a given value of E, the numbers $M_{ij}(E)$ form a table of energy-dependent functions, which we call an M-table, $\mathbf{M}(E)$. For $N = 6$, there are four distinct entries, namely $M_{ii}(E) = \cos 3k = (3E_M/2)(1 - E_M^2/3)$, $M_{i,i+1}(E) = \cos 2k = (E_M^2/2) - 1$, $M_{i,i+2}(E) = \cos k = -E_M/2$, and $M_{i,i+3}(E) = 1$. At $E = E_{HL} = 0$, as expected, this table reveals that the π-orbital contribution to the electrical conductance of meta-connected cores such as $i = 1$ and $j = 3$ is zero, whereas the conductances of para-connected cores ($i = 1$ and $j = 4$) and ortho-connected cores ($i = 1$ and $j = 2$) have the same non-zero conductance. In other words, the conductance ratio $[M_{13}(E_{HL})/M_{14}(E_{HL})]^2$ vanishes, whereas the ratio $[M_{12}(E_{HL})/M_{14}(E_{HL})]^2 = 1$. On the other hand, if E is allowed to vary relative to the H-L gap center, then these ratios change. This example illustrates a property of the M-function (see SI for a list of M-function properties), i.e., that M-functions can be represented by low-order polynomials in E_M, in contrast with Green's functions, which are non-analytic and require infinite power series. Indeed, the above expressions can be written

$$\mathbf{M}(E) = \mathbf{M}(E_{HL}) + \mathbf{M}^{(1)}E_M + \mathbf{M}^{(2)}E_M^2 + \mathbf{M}^{(3)}E_M^3 \tag{3}$$

where $E_{HL} = 0$ and $\mathbf{M}^{(3)} = -{}^1/_2\mathbf{I}$ (with $\mathbf{I}$ the unit matrix), and $\mathbf{M}(E_{HL})$, $\mathbf{M}^{(1)}$, and $\mathbf{M}^{(2)}$ are shown in Figure 2b. This result illustrates another general property of M-functions (see SI), namely that the low-order M-tables $\mathbf{M}^{(1)}$, $\mathbf{M}^{(2)}$, etc. can be constructed from a knowledge of $\mathbf{M}(E_{HL})$ alone. For example, for benzene, the general relationship (see SI) between these tables reduces to $\mathbf{M}^{(1)} = {}^1/_2M^2(E_{HL})$ and $\mathbf{M}^{(2)} = M(E_{HL})\{{}^1/_4[M^2(E_{HL}) - 5]\}$, as can be checked by direct multiplication of $\mathbf{M}(E_{HL})$ in Figure 2b. This means that interference patterns at energies E in the vicinity of the mid-gap can be generated solely from the mid-gap interference patterns $M_{ij}(E_{HL})$.

Equation 2 demonstrates that QI rules established for mid-gap transport are modified when $E \neq E_{HL}$ (i.e., $E_M \neq 0$). For example, at $E_M = 0$, where $M_{ij}(E) = M_{ij}(E_{HL})$, M_{ij} vanishes if i and j are both even or both odd. On the other hand, for finite $E_M \neq 0$, this simple rule is invalid, and instead finite-energy M-tables, as shown in eq 3, should be used.

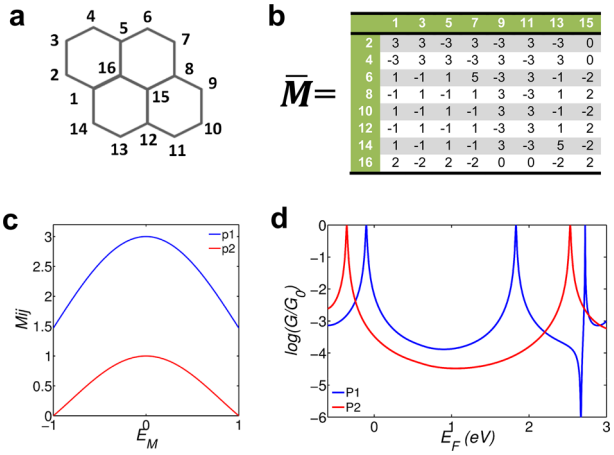

	1	3	5	7	9	11	13	15
2	3	3	-3	3	-3	3	-3	0
4	-3	3	3	-3	3	-3	3	0
6	1	-1	1	5	-3	3	-1	-2
8	-1	1	-1	1	3	-3	1	2
10	1	-1	1	-1	3	3	-1	-2
12	-1	1	-1	1	-3	3	1	2
14	1	-1	1	-1	3	-3	5	-2
16	2	-2	2	-2	0	0	-2	2

Figure 3. Calculated conductances of **P1** and **P2**. (a) Numbering convention for the cores of molecules **P1** and **P2** shown in Figure 1. (b) As noted in eq (35) in the SI, the mid-gap M-table M(0) is block off-diagonal and of the form $\mathbf{M}(0) = \begin{pmatrix} 0 & \bar{M}^t \\ \bar{M} & 0 \end{pmatrix}$. Panel b shows the off-diagonal block $\bar{M}$ of the mid-gap M-table. (c) M-functions of **P1** ($M_{2,9}$) and **P2** ($M_{3,10}$) for energies E varying between the pyrene HOMO (E_H) and the pyrene LUMO (E_L). Both functions are plotted against the dimensionless energy $E_M = (E - E_{HL})/\delta_{HL}$, where $\delta_{HL} = (E_H - E_L)/2$ and $E_{HL} = (E_H + E_L)/2$. The pyrene HOMO (LUMO) corresponds to $E_M = -1$ ($E_M = +1$). (d) NEGF results for the electrical conductance of **P1** and **P2** as a function of the Fermi energy E_F of the electrodes at zero temperature.

Equation 2 is the simplest example of an M-function. It is also a useful starting point for obtaining analytic expressions for M-functions of other PAH cores, such as those shown in Figure 2a, because if the bonds denoted "$-\alpha$" in Figure 2a are set to zero, the peripheral sites of these cores are equivalent to a ring of N sites, whose M-functions are given by eq 2. On the other hand, when $\alpha = \gamma$, electrons traversing the periphery of the ring are scattered at peripheral sites p, labeled p_1, p_2, etc., which are connected by the bonds α. For example, for pyrene, $p_1 = 1$, $p_2 = 5$, $p_3 = 8$, and $p_4 = 12$. Analytic formulas for the resulting M-functions of these lattices are presented in the SI. For pyrene (see eq (25) in the SI), $E_H = -0.45\gamma$, $E_L = 0.45\gamma$, and for naphthalene, $E_H = -0.62\gamma$, $E_L = -0.62\gamma$; as expected, for such bipartite lattices the gap center is at $E_{HL} = 0$. On the other hand, for the non-bipartite azulene (see eq (33) in the SI), $E_H = -0.48\gamma$, $E_L = 0.4\gamma$, and the gap center is at $E_{HL} = -0.04\gamma$. In this case, $E_M = (E + 0.04\gamma)/0.88\gamma$, and $E_M = 0$ does not coincide with 0.

Having introduced the concept of M-functions and energy-dependent M-tables, we now use these to examine mid-gap conductance ratios of molecules with either bipartite or non-bipartite PAH cores. First, we examine the conductance ratios of the pyrene-based molecules **P1** and **P2** shown in Figure 1, which possess bipartite cores and for which $E_{HL} = 0$. Second, we compare the predictions of the MRR with literature measurements for the conductances of other molecules with both bipartite and non-bipartite hearts[38] and with DFT and GW predictions. An analytic formula for the M-functions of a pyrene heart is derived in the SI. The resulting zero-energy M-table $\mathbf{M}(\mathbf{0})$ is block off-diagonal of the form

$$\mathbf{M}(E_{HL}) = \mathbf{M}(\mathbf{0}) = \begin{pmatrix} 0 & \bar{M}^t \\ \bar{M} & 0 \end{pmatrix}$$

DOI: 10.1021/jacs.5b06558
J. Am. Chem. Soc. 2015, 137, 11425−11431

where $\bar{M}$ is a table of integers, as shown in Figure 3b. As examples, $M_{2,9}(E)$ and $M_{3,10}(E)$ are plotted in Figure 3c. These yield, for **P1**, $M_{2,9}(0) = -3$, and for **P2**, $M_{3,10}(0) = -1$. Hence, the MRR predicts a mid-gap conductance ratio of $\sigma_{2,9}/\sigma_{3,10} = (3/1)^2 = 9$.

EXPERIMENTAL AND DFT RESULTS FOR PYRENE

We now verify the above MRR prediction by measuring the electrical conductances of pyrene cores with trimethylsilyl (TMS)-protected acetylene groups at different positions, **P1**[39] and **P2**,[40] using the MCBJ technique.[41] The repeated opening and breaking cycles are carried out in a solution containing 0.1 mM target molecules in a mixture of THF:TMB (mesitylene) = 1:4 (v:v). Then 0.2 mM tetrabutylammonium (TBAF) in a mixture of THF:TMB = 1:4 (v:v) solution was added for *in situ* cleavage reaction of the TMS protecting group.[42,43] Figure 1 shows the schematics of the **P1** and **P2** molecular junctions via the anchoring through a C−Au bond between the two gold electrodes.

Figure 4a shows some typical individual stretching traces from the MCBJ measurement of **P1** and **P2** molecules. For both molecules, current−voltage traces were found to be linear. A sharp conductance decrease occurs after the rupture of gold−gold atomic contacts (plateau at conductance quantum G_0), followed by clear but tilted molecular plateaus for the individual traces. Based on 1000 individual traces, the conductance histograms were constructed without data selection, as shown in Figure 4b. The most probable conductance of **P1** locates at $10^{-3.3\pm0.1}G_0$, while the most probable conductance of **P2** is almost 1 order of magnitude lower at $10^{-4.2\pm0.1}G_0$.

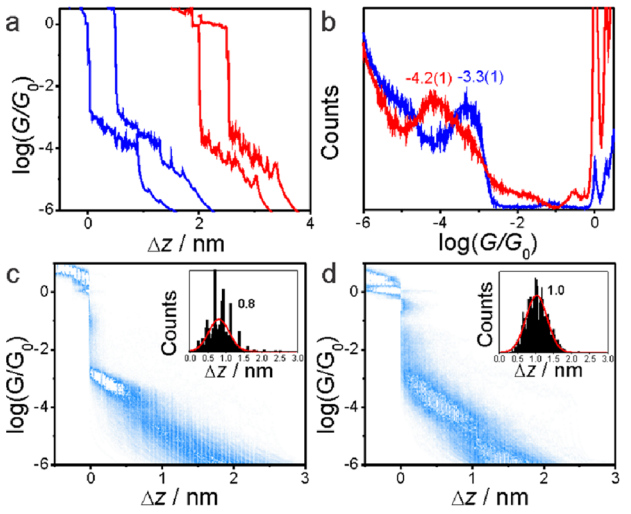

Figure 4. Measured conductances of **P1** and **P2**. (a) Typical conductance−relative distance traces and (b) one-dimensional (1D) conductance histograms of **P1** (blue) and **P2** (red) molecules. (c,d) Two-dimensional (2D) conductance histograms and stretching distance distributions (inset) of **P1** (c) and **P2** (d).

The two-dimensional (2D) histograms in Figure 4c,d reveal that the molecular plateaus are observed in almost all stretching traces, suggesting a ∼100% junction formation probability by the *in situ* cleaving off reaction of the TMS groups, which agrees well with the previous study using the TMS cleaving-off reaction for the formation of a single-molecule junction.[42] The stretching distance distributions of the two molecules (insets of Figure 4c,d) suggest a 0.2 nm difference between the two molecules, which is in good agreement with X-ray structural data, giving Si−Si separations of 14.5 Å (**P1**) (see SI) and 16.0 Å (**P2**),[40] respectively. The experimental conductance ratio of $10^{-3.3}/10^{-4.2}$ is approximately 8, which compares favorably with the MRR prediction of 9. The occurrence of tilted plateaus for both molecules suggests that, during the stretching process, due to the enhanced strength of the Au−C interaction, a single gold atom is detached from the electrode surface, while the gold−carbon bond does not break.[44]

To further verify the MRR prediction, Figure 3d shows the electrical conductances of **P1** and **P2** as a function of the Fermi energy E_F of the electrodes, obtained from a transport calculation using a combination of density functional theory (DFT) and non-equilibrium Green's functions (NEGF) (see Computational Methods). From these results, the predicted conductance ratio varies between 10 and 7 over the range $0 < E_F < 1.2$ and achieves a value of 9 at $E_F = 0.05$, which is close to the DFT-predicted Fermi energy of $E_F = 0$.

COMPARISON WITH LITERATURE RESULTS

Pyrene possesses a bipartite heart, in which atoms labeled by even integers are connected only to atoms labeled by odd integers and the numbers of odd- and even-numbered atoms are equal. We now show that M-functions describe non-bipartite lattices such as azulene, whose M-functions have no particular symmetry and whose values at the gap center are not integers. This molecule is a challenge, because well-known bond counting rules for predicting QI[45,46] have been shown to

Table 1. (Top) Comparison of the Mid-gap Ratio Rule (MRR), GW Prediction, and Experimental Conductance Ratios for Azulene, Obtained by Dividing by the Conductance or M-Function of the 8,10 Connectivity; (Bottom) Comparisons with Experimental Results from the Literature and with Our Experimental Results for Pyrene[a]

molecular heart	anchor group	connectivities	literature notation	MRR	exptl ratio	GW prediction[b]	DFT prediction
azulene	thiochroman	4,9/8,10	ratio of molecules **2,6,AZ** and **1,3,AZ** of ref 38	0.72	1	0.32	0.93
azulene	thiochroman	6,3/8,10	ratio of molecules **4,7,AZ** and **1,3,AZ** of ref 38	0.79	0.25	0.32	0.13
azulene	thiochroman	3,5/8,10	ratio of molecules **5,7,AZ** and **1,3,AZ** of ref 38	0.003	0.06	0.1	0.05
naphthalene	thiol	7,10/3,8	ratio of molecules **4** and **6** of ref 15	4	5.1	na[c]	2
anthracene	thiol	see SI	ratio of molecules **5** and **7** of ref 15	16	10.2	na[c]	13
pyrene	carbon	2,9/3,10	**P1** and **P2** of this paper	9	8	na[c]	9
anthanthrene	pyridyl	see SI	ratio of molecules **1** and **2** of ref 2	81	79	na[c]	81

[a]It is interesting to note that the mean-square deviations (χ^2) of the MRR and GW predictions from the experimental azulene data are 0.37 and 0.44, respectively, which reveals that, despite its simplicity, the accuracy of the MRR is comparable with that of the GW calculation. [b]Ref 38. [c]Not available.

DOI: 10.1021/jacs.5b06558
J. Am. Chem. Soc. 2015, 137, 11425−11431

break down in azulene cores.[38] Four examples—$M_{8,10}(E)$, $M_{4,9}(E)$, $M_{3,6}(E)$, and $M_{3,5}(E)$—of the analytic formula (see SI) for azulene M-functions are plotted in Figure S1c in the SI. These examples allow us to test the MRR against measurements of the electrical conductance of molecules with azulene cores,[38] where it was reported that $\sigma_{8,10} = 32 \times 10^{-5} G_0$, $\sigma_{4,9} = 32 \times 10^{-5} G_0$, $\sigma_{3,6} = 8 \times 10^{-5} G_0$, and $\sigma_{3,5} = 2 \times 10^{-5} G_0$, yielding experimental conductance ratios of $\sigma_{4,9}/\sigma_{8,10} = 1$, $\sigma_{5,8}/\sigma_{8,10} = 1/4$, and $\sigma_{3,5}/\sigma_{8,10} = 1/16$.

Table 1 shows a comparison between MRR and experiment, and demonstrates good agreement between the experiment and our parameter-free MRR. For example, the ratio between connectivities 4,9 and 8,10 of azulene is measured to be 1, whereas the GW calculation[38] and our DFT-NEGF calculation yield ratios of 0.32 and 0.93, respectively. These predictions were obtained by treating the Fermi energy as a free parameter and adjusting it to yield the closest agreement with experiment. For example, in the GW calculations, the Fermi energy is chosen to be far from the GW-predicted Fermi energy (−1.5 eV). In contrast, our parameter-free MRR, which has no such freedom, predicts a ratio of 0.72, in much better agreement with the experiment. For completeness, Table 1 also shows excellent agreement between the parameter-free MRR and existing experimental values for naphthalene,[15] anthracene,[15] and anthanthrene.[2]

The above result is remarkable, because if the Fermi energy E_F of external electrodes does not coincide with the mid-gap E_{HL}, then the MRR should be replaced by

$$\sigma_{i,j}/\sigma_{l,m} = [M_{i,j}(E_F)/M_{l,m}(E_F)]^2 \quad (4)$$

The fact that the MRR agrees with experiment suggests that, in all of the above measurements, E_F is close to the mid-gap.

PHASE-COHERENT INTERFEROMETERS AND LOGIC GATES

The MRR is derived under the assumption that transport through a molecule is phase-coherent, and since the agreement in Table 1 between theory and experiment suggests that this assumption is correct, it is natural to utilize M-tables in the design of devices with more complex connectivities. In what follows, we examine theoretical concepts underpinning phase-coherent logic gates and transport through three-terminal devices, which illustrate the significance of the signs of the M-table entries.

In a three-terminal device with phase-coherent inputs of amplitudes A_j and A_k, and an output site j', the electrical conductance $\sigma_{jk;jj'}$ is proportional to $|A_j M_{jj'} + A_k M_{kj'}|^2$ rather than $|A_j M_{jj'}|^2 + |A_k M_{kj'}|^2$. This leads to strategies for designing phase-coherent transistors and logic gates and optimizing the sensitivity of molecular-scale Aharonov−Bohm (A-B) interferometers. As an example, Figure 5a shows a pyrene-based XOR gate, whose truth table (Figure 5b) is obtained from the fact that, from the M-table of Figure 3b, $M_{4,9} = -M_{2,9} = 3$, which means that the conductance between connectivities 2,9 or 4,9 alone would be proportional to $|\pm 3|^2 = 9$ whereas if both inputs (2 and 4) are "on", then the conductance would vanish $|+3-3|^2 = 0$. Clearly, higher order logic gates could be obtained by combining elementary functions such as these. If the core of a molecule is gated by a third electrode, such that E_F no longer coincides with the mid-gap, then the signs of M-functions at non-mid-gap energies are relevant, and the electrical conductance is proportional to $\sigma_{jk;jj'}(E_F) = |M_{jj'}(E_F) + M_{kj'}(E_F)|^2$.

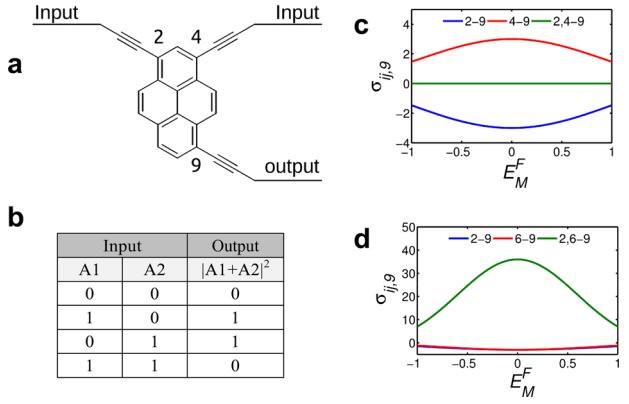

Input		Output
A1	A2	$\|A1+A2\|^2$
0	0	0
1	0	1
0	1	1
1	1	0

Figure 5. Pyrene-based phase-coherent XOR gate. (a) Connections 2,9 and 4,9, with M numbers of opposite sign and equal magnitude, and (b) the resulting truth table. (c) The Fermi energy dependence of M_{29} (blue), M_{49} (red), and $\sigma_{2,4;9}$ (green). (d) The Fermi energy dependence of M_{29} (blue), M_{69} (red), and $\sigma_{2,6;9}$ (green). All quantities are plotted against the dimensionless Fermi energy, $E_M^F = (E_F - E_{HL})/\delta_{HL}$.

For the three-fold connectivity of Figure 5a, Figure 5c,d shows a plot of the electrical conductances $\sigma_{2,4;9}(E_F)$ and $\sigma_{2,6;9}(E_F)$ versus E_F and demonstrates that M-functions provide insight into the gate dependence of multiply connected cores and can be used to select connectivities that enhance or reduce the sensitivity to electrostatic gating. Since reproducible three-terminal devices are not currently available in the laboratory, we illustrate the use of M-functions in three-terminal devices through a theoretical study of molecular-scale A-B effect and a molecular-scale logic gate.

A schematic of an A-B device in which a top electrode is connected to a metallic loop, through which a magnetic flux is passed, is shown in Figure 6a. The loop connects to two sites, j

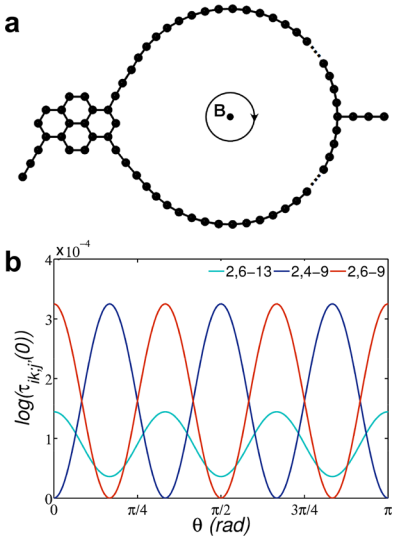

Figure 6. (a) Schematic of an Aharonov−Bohm loop in which the two arms of the loop are connected to different atoms of the pyrene core. A magnetic field **B** creates a flux φ through the loop and a relative phase shift $\theta = 2\pi\varphi/\varphi_0$ for partial de Broglie waves traversing the different arms. (b) Electrical conductance as a function of the dimensionless flux θ for the different connection points to the pyrene core. The largest amplitude (i.e., flux sensitivity) occurs for the connectivities $\sigma_{2,4;9}$ and $\sigma_{2,6;9}$.

DOI: 10.1021/jacs.5b06558
J. Am. Chem. Soc. 2015, 137, 11425−11431

and k, and the current exits through a bottom electrode connected to site j'. For incoming waves whose amplitudes differ only by a phase θ, mid-gap electrical conductance is proportional to $\sigma_{jk;j'} = |M_{jj'}(E_{HL}) + e^{i\theta}M_{kj'}(E_{HL})|^2$. If j, k, and j' are chosen to be 2, 6, and 13, then since $M_{2,13}(E_{HL}) = -3$ and $M_{6,13}(E_{HL}) = -1$, this yields $\sigma_{2,6;13} = |-3 + (-1)e^{i\theta}|^2 = 10 + 6\cos(\theta)$, and therefore the amplitude of oscillation (12) is 12/16 = 75% of the maximum value. The green curve in Figure 6 shows the result of a complete tight-binding calculation of the conductance versus magnetic flux through the loop φ in units of the flux quantum φ_0. This is related to the phase θ by $\theta = 2\pi\varphi/\varphi_0$.

To illustrate how M-tables can be utilized in improving the sensitivity of such interferometers, we now seek to increase this amplitude to 100%. From the M-table, the solution is immediately obvious, because $M_{2,9}(E_{HL}) = -3$ and $M_{6,9}(E_{HL}) = -3$; therefore, if j, k, and j' are chosen to be 2, 6, and 9, one obtains $\sigma_{2,6;9} = |-3 - 3e^{i\theta}|^2 = 18 + 18\cos(\theta)$, yielding a 100% amplitude. On the other hand, since $M_{2,9}(E_{HL}) = -3$ and $M_{4,9}(E_{HL}) = +3$, if j, k, and j' are chosen to be 2, 4, and 9, one obtains $\sigma_{2,4;9} = |-3 - 3e^{i\theta}|^2 = 18 - 18\cos(\theta)$, and therefore a π-shifted interferometer with a 100% amplitude is obtained. These features are demonstrated by performing a tight-binding calculation (see Computational Methods) of the structure of Figure 6a, the result of which is shown in Figure 6b.

CONCLUSION

When electrons enter the heart of a PAH at site j, then provided the coupling to the linkers is sufficiently weak, the amplitude of the resulting de Broglie wave at site i is proportional to the M-function $M_{ij}(E)$. Although the associated electrical conductance $\sigma_{i,j}$ depends on the nature of the coupling to the electrodes, the ratio of two such conductances with different choices of i and j does not. We have shown that mid-gap M-functions correctly predict conductance ratios of molecules with bipartite cores such as pyrene and non-bipartite cores such as azulene. Despite the simplicity of this parameter-free theory, quantitative agreement with experiment, with density functional theory, and with many-body GW calculations was obtained. One of the reasons for this agreement is that the MRR is independent of the energy gap of the molecules. Therefore, even though a nearest-neighbor tight-binding model may not be capable of describing the band gap for some large PAHs, where hydrogen-induced edge distortion is important (see, for instance, ref 47), conductance ratios are correctly predicted.

Since energy-dependent M-functions can be obtained from gap-center M-tables, this agreement between gap-center values and experiment gives us confidence that M-functions correctly predict the energy dependence of interference patterns and superpositions of these patterns in multiply connected molecules. As demonstrations of their utility, we have shown that M-functions can be used to design phase-coherent logic gates and to optimize the sensitivity of molecular A-B and electrostatically gated interferometers. The concept of energy-dependent M-functions is general and, in contrast with theories of transport resonances, focuses attention on the opposite limit of transport in the vicinity of the mid-gap. These functions are properties of a molecular core and generalize QI rules to arbitrary energies within the H-L gap.

COMPUTATIONAL METHODS

The Hamiltonian of the structures described in this paper was obtained using DFT as described below or constructed from a simple tight-binding model with a single orbital per atom of site energy $\varepsilon_0 = 0$ and nearest-neighbor couplings $\gamma = -1$. To calculate the A-B effect, for the different connection points to the pyrene (Figure 6), the A-B loop is a ring of 11 atoms, with $\varepsilon_{\text{A-B loop}} = 0.05$ and $\gamma_{\text{A-B loop}} = -e^{i\theta}$, where θ varies in the interval of $[0,\pi]$.

Density Functional Theory (DFT) Calculation. The optimized geometry and ground-state Hamiltonian and overlap matrix elements of each structure were obtained self-consistently using the *SIESTA*[48] implementation of DFT. *SIESTA* employs norm-conserving pseudopotentials to account for the core electrons and linear combinations of atomic orbitals to construct the valence states. The generalized gradient approximation (GGA) of the exchange and correlation functional is used with the Perdew–Burke–Ernzerhof (PBE) parametrization,[49] a double-ζ polarized (DZP) basis set, and a real-space grid defined with an equivalent energy cutoff of 250 Ry. Geometry optimization for each structure is performed until the forces are smaller than 40 meV/Å.

DFT-NEGF Transport Calculation. The mean-field Hamiltonian obtained from the converged DFT calculation or a simple tight-binding Hamiltonian was combined with our implementation of the NEGF method, the *GOLLUM*,[50] to calculate the phase-coherent elastic scattering properties of the each system consisting of left (source) and right (drain) leads and the scattering region. The transmission coefficient $T(E)$ for electrons of energy E (passing from the source to the drain) is calculated via the relation $T(E) = \text{Tr}[\Gamma_R(E)G^R(E)\Gamma_L(E)G^{R\dagger}(E)]$. In this expression, $\Gamma_{L,R}(E) = i[\sum_{L,R}(E) - \sum_{L,R}^{\dagger}(E)]$ describes the level broadening due to the coupling between left (L) and right (R) electrodes and the central scattering region, $\sum_{L,R}(E)$ are the retarded self-energies associated with this coupling, and $G^R = (E\mathbf{S} - \mathbf{H} - \sum_L - \sum_R)^{-1}$ is the retarded Green's function, where $\mathbf{H}$ is the Hamiltonian and $\mathbf{S}$ is the overlap matrix. Using the obtained transmission coefficient $T(E)$, the conductance could be calculated[51] by the Landauer formula, $G = G_0\int dE T(E)(-\partial f/\partial E)$, where $G_0 = 2e^2/h$ is the conductance quantum and $f(E) = (1 + \exp[(E - E_F)/k_BT])^{-1}$ is the Fermi–Dirac distribution function, T is the temperature, and $k_B = 8.6 \times 10^{-5}$ eV/K is the Boltzmann's constant.

Analytical Methods. M-functions are related to the Green's function of an isolated core by $M_{i,j}(E) = D(E)G_{i,j}(E)$, where $D(E)$ is proportional to $\det(E - H)$, divided by a polynomial to remove degenerate eigenvalues. Since we are only interested in sites i,j which can be connected by linkers to external electrodes, we solve Dyson's equation to obtain the "peripheral Green's function" $G_{i,j}(E)$ connecting only sites on the periphery of a core (see SI).

ASSOCIATED CONTENT

Supporting Information

The Supporting Information is available free of charge on the ACS Publications website at DOI: 10.1021/jacs.5b06558.

X-ray crystallographic data for **P1** (CIF)

Description of the relationship between M-functions and Green's functions; summary of the properties of M-functions; derivations of analytic formulas for Green's functions and M-functions of the molecules of Figure 2; plots of M-functions of these and a more complex tetracene-based "cross molecule"; method of computing finite energy M-functions from mid-gap M-tables; expression for the core transmission coefficient (PDF)

AUTHOR INFORMATION

Corresponding Authors

*s.sangtarash@lancaster.ac.uk

*hong@dcb.unibe.ch

*liu@dcb.unibe.ch

DOI: 10.1021/jacs.5b06558
J. Am. Chem. Soc. 2015, 137, 11425–11431

*c.lambert@lancaster.ac.uk

Author Contributions

§S.S., C.H., and H.S. contributed equally to this work.

Notes

The authors declare no competing financial interest.

■ ACKNOWLEDGMENTS

This work was supported by the Swiss National Science Foundation (no. 200021-147143) as well as by the European Commission (EC) FP7 ITN "MOLESCO" (project no. 606728) and UK EPSRC (grant nos. EP/K001507/1, EP/J014753/1, and EP/H035818/1).

■ REFERENCES

(1) Lambert, C. *Chem. Soc. Rev.* **2015**, *44*, 875.
(2) Geng, Y.; Sangtarash, S.; Huang, C.; Sadeghi, H.; Fu, Y.; Hong, W.; Wandlowski, T.; Decurtins, S.; Lambert, C. J.; Liu, S.-X. *J. Am. Chem. Soc.* **2015**, *137*, 4469.
(3) Sadeghi, H.; Mol, J. A.; Lau, C. S.; Briggs, G. A. D.; Warner, J.; Lambert, C. J. *Proc. Natl. Acad. Sci. U. S. A.* **2015**, *112*, 2658.
(4) Sedghi, G.; García-Suárez, V. M.; Esdaile, L. J.; Anderson, H. L.; Lambert, C. J.; Martín, S.; Bethell, D.; Higgins, S. J.; Elliott, M.; Bennett, N. *Nat. Nanotechnol.* **2011**, *6*, 517.
(5) Zhao, X.; Huang, C.; Gulcur, M.; Batsanov, A. S.; Baghernejad, M.; Hong, W.; Bryce, M. R.; Wandlowski, T. *Chem. Mater.* **2013**, *25*, 4340.
(6) Magoga, M.; Joachim, C. *Phys. Rev. B: Condens. Matter Mater. Phys.* **1999**, *59*, 16011.
(7) Papadopoulos, T.; Grace, I.; Lambert, C. *Phys. Rev. B: Condens. Matter Mater. Phys.* **2006**, *74*, 193306.
(8) Bergfield, J. P.; Solis, M. A.; Stafford, C. A. *ACS Nano* **2010**, *4*, 5314.
(9) Ricks, A. B.; Solomon, G. C.; Colvin, M. T.; Scott, A. M.; Chen, K.; Ratner, M. A.; Wasielewski, M. R. *J. Am. Chem. Soc.* **2010**, *132*, 15427.
(10) Markussen, T.; Schiötz, J.; Thygesen, K. S. *J. Chem. Phys.* **2010**, *132*, 224104.
(11) Solomon, G. C.; Bergfield, J. P.; Stafford, C. A.; Ratner, M. A. *Beilstein J. Nanotechnol.* **2011**, *2*, 862.
(12) Vazquez, H.; Skouta, R.; Schneebeli, S.; Kamenetska, M.; Breslow, R.; Venkataraman, L.; Hybertsen, M. *Nat. Nanotechnol.* **2012**, *7*, 663.
(13) Ballmann, S.; Härtle, R.; Coto, P. B.; Elbing, M.; Mayor, M.; Bryce, M. R.; Thoss, M.; Weber, H. B. *Phys. Rev. Lett.* **2012**, *109*, 056801.
(14) Aradhya, S. V.; Meisner, J. S.; Krikorian, M.; Ahn, S.; Parameswaran, R.; Steigerwald, M. L.; Nuckolls, C.; Venkataraman, L. *Nano Lett.* **2012**, *12*, 1643.
(15) Kaliginedi, V.; Moreno-García, P.; Valkenier, H.; Hong, W.; García-Suárez, V. M.; Buiter, P.; Otten, J. L.; Hummelen, J. C.; Lambert, C. J.; Wandlowski, T. *J. Am. Chem. Soc.* **2012**, *134*, 5262.
(16) Aradhya, S. V.; Venkataraman, L. *Nat. Nanotechnol.* **2013**, *8*, 399.
(17) Arroyo, C. R.; Tarkuc, S.; Frisenda, R.; Seldenthuis, J. S.; Woerde, C. H.; Eelkema, R.; Grozema, F. C.; van der Zant, H. S. *Angew. Chem.* **2013**, *125*, 3234.
(18) Guédon, C. M.; Valkenier, H.; Markussen, T.; Thygesen, K. S.; Hummelen, J. C.; van der Molen, S. J. *Nat. Nanotechnol.* **2012**, *7*, 305.
(19) Ke, S.-H.; Yang, W.; Baranger, H. U. *Nano Lett.* **2008**, *8*, 3257.
(20) Venkataraman, L.; Klare, J. E.; Tam, I. W.; Nuckolls, C.; Hybertsen, M. S.; Steigerwald, M. L. *Nano Lett.* **2006**, *6*, 458.
(21) Quek, S. Y.; Venkataraman, L.; Choi, H. J.; Louie, S. G.; Hybertsen, M. S.; Neaton, J. B. *Nano Lett.* **2007**, *7*, 3477.
(22) Dell'Angela, M.; Kladnik, G.; Cossaro, A.; Verdini, A.; Kamenetska, M.; Tamblyn, I.; Quek, S. Y.; Neaton, J. B.; Cvetko, D.; Morgante, A.; Venkataraman, L. *Nano Lett.* **2010**, *10*, 2470.
(23) Quek, S. Y.; Kamenetska, M.; Steigerwald, M. L.; Choi, H. J.; Louie, S. G.; Hybertsen, M. S.; Neaton, J. B.; Venkataraman, L. *Nat. Nanotechnol.* **2009**, *4*, 230.
(24) Bagrets, A.; Arnold, A.; Evers, F. *J. Am. Chem. Soc.* **2008**, *130*, 9013.
(25) Stadler, R.; Thygesen, K. S.; Jacobsen, K. W. *Phys. Rev. B: Condens. Matter Mater. Phys.* **2005**, *72*, 241401.
(26) Wang, C.; Batsanov, A. S.; Bryce, M. R.; Martín, S.; Nichols, R. J.; Higgins, S. J.; García-Suárez, V. M.; Lambert, C. J. *J. Am. Chem. Soc.* **2009**, *131*, 15647.
(27) Kim; Beebe, J. M.; Jun, Y.; Zhu, X. Y.; Frisbie, C. D. *J. Am. Chem. Soc.* **2006**, *128*, 4970.
(28) Chen, F.; Li, X.; Hihath, J.; Huang, Z.; Tao, N. *J. Am. Chem. Soc.* **2006**, *128*, 15874.
(29) Schull, G.; Frederiksen, T.; Arnau, A.; Sanchez-Portal, D.; Berndt, R. *Nat. Nanotechnol.* **2011**, *6*, 23.
(30) Martin, C. A.; Ding, D.; Sørensen, J. K.; Bjørnholm, T.; van Ruitenbeek, J. M.; van der Zant, H. S. J. *J. Am. Chem. Soc.* **2008**, *130*, 13198.
(31) Chen, F.; Tao, N. *Acc. Chem. Res.* **2009**, *42*, 429.
(32) Pisula, W.; Feng, X.; Müllen, K. *Chem. Mater.* **2011**, *23*, 554.
(33) Wu, J.; Pisula, W.; Müllen, K. *Chem. Rev.* **2007**, *107*, 718.
(34) Coskun, A.; Spruell, J. M.; Barin, G.; Dichtel, W. R.; Flood, A. H.; Botros, Y. Y.; Stoddart, J. F. *Chem. Soc. Rev.* **2012**, *41*, 4827.
(35) Al-Galiby, Q.; Grace, I.; Sadeghi, H.; Lambert, C. J. *J. Mater. Chem. C* **2015**, *3*, 2101.
(36) Ruffieux, P.; Cai, J.; Plumb, N. C.; Patthey, L.; Prezzi, D.; Ferretti, A.; Molinari, E.; Feng, X.; Müllen, K.; Pignedoli, C. A. *ACS Nano* **2012**, *6*, 6930.
(37) Cai, J.; Pignedoli, C. A.; Talirz, L.; Ruffieux, P.; Söde, H.; Liang, L.; Meunier, V.; Berger, R.; Li, R.; Feng, X. *Nat. Nanotechnol.* **2014**, *9*, 896.
(38) Xia, J.; Capozzi, B.; Wei, S.; Strange, M.; Batra, A.; Moreno, J. R.; Amir, R. J.; Amir, E.; Solomon, G. C.; Venkataraman, L.; Campos, L. M. *Nano Lett.* **2014**, *14*, 2941.
(39) Ohshita, J.; Yoshimoto, K.; Tada, Y.; Harima, Y.; Kunai, A.; Kunugi, Y.; Yamashita, K. *J. Organomet. Chem.* **2003**, *678*, 33.
(40) Crawford, A. G.; Liu, Z.; Mkhalid, I. A. I.; Thibault, M.-H.; Schwarz, N.; Alcaraz, G.; Steffen, A.; Collings, J. C.; Batsanov, A. S.; Howard, J. A. K.; Marder, T. B. *Chem. - Eur. J.* **2012**, *18*, 5022.
(41) Hong, W.; Valkenier, H.; Mészáros, G.; Manrique, D. Z.; Mishchenko, A.; Putz, A.; García, P. M.; Lambert, C. J.; Hummelen, J. C.; Wandlowski, T. *Beilstein J. Nanotechnol.* **2011**, *2*, 699.
(42) Hong, W.; Li, H.; Liu, S.-X.; Fu, Y.; Li, J.; Kaliginedi, V.; Decurtins, S.; Wandlowski, T. *J. Am. Chem. Soc.* **2012**, *134*, 19425.
(43) Fu, Y.; Chen, S.; Kuzume, A.; Rudnev, A.; Huang, C.; Kaliginedi, V.; Baghernejad, M.; Hong, W.; Wandlowski, T.; Decurtins, S.; Liu, S.-X. *Nat. Commun.* **2015**, *6*, 6403−6409.
(44) Hoft, R. C.; Ford, M. J.; García-Suárez, V. M.; Lambert, C. J.; Cortie, M. B. *J. Phys.: Condens. Matter* **2008**, *20*, 025207.
(45) Markussen, T.; Stadler, R.; Thygesen, K. S. *Nano Lett.* **2010**, *10*, 4260.
(46) Yoshizawa, K.; Tada, T.; Staykov, A. *J. Am. Chem. Soc.* **2008**, *130*, 9406.
(47) Gunlycke, D.; White, C. T. *Phys. Rev. B: Condens. Matter Mater. Phys.* **2008**, *77*, 115116.
(48) Soler, J. M.; Artacho, E.; Gale, J. D.; García, A.; Junquera, J.; Ordejón, P.; Sánchez-Portal, D. *J. Phys.: Condens. Matter* **2002**, *14*, 2745.
(49) Perdew, J. P.; Burke, K.; Ernzerhof, M. *Phys. Rev. Lett.* **1996**, *77*, 3865.
(50) Ferrer, J.; Lambert, C.; Garcia-Suarez, V.; Zsolt Manrique, D.; Visontai, D.; Oroszlani, L.; Ferradás, R.; Grace, I.; Bailey, S.; Gillemot, K.; Sadeghi, H.; Algharagholy, L. *New J. Phys.* **2014**, *16*, 093029.
(51) Sadeghi, H.; Sangtarash, S.; Lambert, C. J. *Sci. Rep.* **2015**, *5*, 9514.

DOI: 10.1021/jacs.5b06558
J. Am. Chem. Soc. 2015, 137, 11425−11431